


Oscillating edge current in polar active fluid

Hiroki Matsukiyo (松清洋輝)  and Jun-ichi Fukuda (福田順一) 

Department of Physics, Kyushu University, 744 Motoooka, Nishi-ku, Fukuoka 819-0395, Japan

 (Received 30 November 2023; accepted 11 April 2024; published 14 May 2024; corrected 28 June 2024)

Dense bacterial suspensions exhibit turbulent behavior called bacterial turbulence. The behavior of the bulk unconstrained bacterial turbulence is described well by the Toner-Tu-Swift-Hohenberg (TTSH) equation for the velocity field. However, it remains unclear how we should treat boundary conditions on bacterial turbulence in contact with some boundaries (e.g., solid walls). To be more specific, although the importance of the edge current, the flow along the boundary, has been demonstrated in several experimental studies on confined bacterial suspensions, previous numerical studies based on the TTSH equation employ nonslip boundary conditions and do not seem to properly describe the behavior of bacteria near the boundaries. In this paper, we impose a slip boundary condition on the TTSH equation to describe the bacterial motion at boundaries. We develop a method to implement the slip boundary condition. Using this method, we have successfully produced edge current and discovered that the direction of the edge current temporally oscillates. The oscillation can be attributable to the advection term in the TTSH equation. Our paper demonstrates that boundary conditions could play an important role in the collective dynamics of active systems.

DOI: [10.1103/PhysRevE.109.054604](https://doi.org/10.1103/PhysRevE.109.054604)

I. INTRODUCTION

Turbulence-like behavior is observed in a wide range of active matter systems. It is called active turbulence (for an inclusive review, see Ref. [1]). As listed in Ref. [1], active turbulence has been reported in various kinds of experimental systems, such as sperm suspensions [2], self-propelled Janus particles [3], tissue cell monolayers [4], microtubule-kinesin suspensions [5,6], etc.

Dense bacterial suspensions also exhibit turbulent behavior called bacterial turbulence [1,7,8]. Bacterial turbulence has a characteristic size of vortex, larger than the size of each single bacterium, and then exhibits a peaked energy spectrum. Such characteristic velocity and vorticity profiles and energy spectrum are well-described by the Toner-Tu-Swift-Hohenberg (TTSH) equation [1,7,8] in which the coarse-grained collective velocity field \mathbf{v} , which is given by the sum of the velocity of the solvent fluid and that of the swimmers with respect to the fluid [9,10], is considered as the only field variable describing the state of the system, and other degrees of freedom (polar order, orientational order, density) are not taken into account (for example, orientational order is assumed to be parallel to \mathbf{v}). The TTSH equation is given by

$$(\partial_t + \lambda_0 \mathbf{v} \cdot \nabla) \mathbf{v} = -\nabla p + \lambda_1 \nabla(\mathbf{v}^2) - (\alpha + \beta |\mathbf{v}|^2) \mathbf{v} + \Gamma_0 \nabla^2 \mathbf{v} - \Gamma_2 (\nabla^2)^2 \mathbf{v} \quad (1)$$

and the incompressibility condition:

$$\nabla \cdot \mathbf{v} = 0. \quad (2)$$

In Eq. (1), λ_0 , λ_1 , α , β , Γ_0 , and Γ_2 are constants determined phenomenologically and p is the Lagrange multiplier to ensure the incompressibility [Eq. (2)]. The TTSH model does not explicitly take account of the solvent in which bacteria swim [1], and therefore breaks the Galilean invariance,

which is reflected in the presence of the λ_0 ($\neq 1$), λ_1 , α , and β terms. The term $-(\alpha + \beta |\mathbf{v}|^2) \mathbf{v}$, called the Toner-Tu term, gives a characteristic speed $v_0 = \sqrt{|\alpha|/\beta}$ and the term $\Gamma_0 \nabla^2 \mathbf{v} - \Gamma_2 (\nabla^2)^2 \mathbf{v}$, called the Swift-Hohenberg term, gives a characteristic length scale $\Lambda_0 = 2\pi \sqrt{2\Gamma_2/|\Gamma_0|}$.

In recent years, control of the bacterial turbulence has been attracting interest. More specifically, by imposing geometrical confinements on bacterial suspensions (e.g., confining bacterial suspensions in microscopic devices, locating small obstacles in bacterial suspensions, etc.), it has been shown that the seemingly chaotic motions of bacterial turbulence can be rectified in many experimental systems: Wioland *et al.* [11] confined bacterial suspensions into chambers connected by channels and demonstrated the transition between ferromagnetic and antiferromagnetic vortex order (where the directions of the adjacent vortices are the same and different, respectively) by varying the width of channels. Beppu *et al.* [12] performed experiments using dumbbell-shaped devices and showed a ferro-antiferromagnetic vortex order transition by varying the distance between the centers of the two circles. Nishiguchi *et al.* [13] realized antiferromagnetic vortex order by locating, in bacterial suspensions, periodic arrays of microscopic vertical pillars whose lateral size is comparable with the length of a single bacterium.

To study such systems numerically, it is natural to apply the TTSH equation to the situations where some boundaries exist. There already exist several studies along this direction: Reinken *et al.* [14,15] suggested a numerical method to implement many small obstacles located in bacterial turbulence and obtained the results consistent with experiments. Puggioni *et al.* [16,17] performed TTSH simulations in confined circular domains whose radius was much larger than the typical vortex size and showed emergence of a giant vortex whose size was comparable with the circular domains. Shiratani *et al.* [18] also performed simulations in which the radius of the

circular domain was varied with time, and discovered a hysteresis of the transition between the single-vortex stationary state and the vortex-pair oscillatory state.

As stated above, the previous TTSH simulations revealed several interesting phenomena. However, the simulation methods used there seem to fail to capture the behavior at boundaries because they cannot realize edge current, i.e., the bacterial flow along the boundaries.

Edge current emerging in various active systems (bacterial suspensions [19], active nematics [20,21], active spinner materials [22,23], etc.) has been attracting interest recently. In this paper, we particularly focus on bacterial suspensions described by the TTSH model. Several experimental studies on confined bacterial suspensions demonstrated that the edge current gives an essential effect on their collective motion [11,12,19,24]. However, in all the above TTSH simulations [14–18], a damping term is introduced to represent the boundary, and then nonslip boundary condition is imposed. As stated clearly in Ref. [18], in the simulations using nonslip boundary condition, the magnitude of the velocity continuously decays to zero at the boundaries due to the damping terms and the edge current does not emerge. Therefore a nonslip boundary condition does not properly describe the bacterial motion at the boundaries.

In this paper, we investigate how the difference of boundary conditions affects bacterial collective dynamics. We propose an extended TTSH model to implement the slip boundary condition (Sec. II) and, furthermore, present a numerical method to calculate our extended model equations (Sec. III). As a result of simulations, we have successfully realized the edge current (Sec. IV). Furthermore, we discovered that the direction of the edge current temporally oscillates (Sec. IV). Note that we consider the two-dimensional TTSH equation in this paper.

II. MODEL

To describe the bacterial dynamics, we use the Toner-Tu-Swift-Hohenberg (TTSH) equation [1,7,8] [Eqs. (1) and (2)], already mentioned in Sec. I. Note that the λ_1 term in Eq. (1) can be absorbed into the p term: $-\nabla p + \lambda_1 \nabla(\mathbf{v}^2) = -\nabla(p - \lambda_1 \mathbf{v}^2) \equiv -\nabla q$, where we have introduced a new Lagrange multiplier q . Let us use the TTSH equation without the λ_1 term in the following discussions.

Next, for the following discussions, let us rewrite the TTSH equation [Eq. (1)] in terms of a functional derivative,

$$\partial_t \mathbf{v} = -\frac{\delta \mathcal{F}}{\delta \mathbf{v}} - \lambda_0 \mathbf{v} \cdot \nabla \mathbf{v}, \quad (3)$$

where we have introduced the functional

$$\mathcal{F}[\mathbf{v}] = \int d\mathbf{r} \left\{ -q \partial_i v_i + \frac{\alpha}{2} v_i v_i + \frac{\beta}{4} v_i v_i v_j v_j + \frac{\Gamma_0}{2} (\partial_j v_i)(\partial_j v_i) + \frac{\Gamma_2}{2} (\partial_j \partial_j v_i)(\partial_k \partial_k v_i) \right\}. \quad (4)$$

The first term in Eq. (3), $-\delta \mathcal{F}/\delta \mathbf{v}$, drives the system towards the minimization of the functional \mathcal{F} . The second term, $-\lambda_0 \mathbf{v} \cdot \nabla \mathbf{v}$, is the advective term and λ_0 is the strength of the advection.

To implement the slip boundary condition, we replace the functional \mathcal{F} with \mathcal{F} given by

$$\mathcal{F}[\mathbf{v}] = \int_V d\mathbf{r} \left\{ -q \partial_i v_i + \frac{\alpha}{2} v_i v_i + \frac{\beta}{4} v_i v_i v_j v_j + \frac{\Gamma_0}{2} (\partial_j v_i)(\partial_j v_i) + \frac{\Gamma_2}{2} (\partial_j \partial_j v_i)(\partial_k \partial_k v_i) \right\} + \frac{\xi}{2} \int_S dS (\mathbf{n} \times \mathbf{v})_z^2, \quad (5)$$

where the body integral $\int_V d\mathbf{r}$ is taken over the fluid region, the surface integral $\int_S dS$ is taken over the surface (S) of V , and \mathbf{n} is the outward unit normal vector at the surface S . The surface term $\frac{\xi}{2} \int_S dS (\mathbf{n} \times \mathbf{v})_z^2$ can be regarded as the energetic penalty for the slip velocity $(\mathbf{n} \times \mathbf{v})_z$. $\xi (> 0)$ is the drag coefficient. When $\xi = 0$, no penalty arises for any finite slip velocity and the functional $\mathcal{F}[\mathbf{v}]$ gives a stress-free slip boundary condition. On the other hand, when $\xi \rightarrow \infty$, an infinite penalty arises for arbitrary finite slip velocity and the functional $\mathcal{F}[\mathbf{v}]$ gives nonslip boundary condition (see Appendix C). The boundary condition for a finite value of ξ will be discussed in Sec. III B after specifying the shape of the boundary.

III. NUMERICAL METHOD

A. Smoothed profile method

To solve the extended model [Eq. (3) with the functional $\mathcal{F}[\mathbf{v}]$, given by Eq. (5)] numerically, we use the smoothed profile method (SPM) [25,26], where fluid-solid boundaries are represented by the smoothed profile ϕ :

$$\phi = \begin{cases} 0 & \text{in solid regions} \\ \text{varies between 0 and 1 smoothly} & \text{at boundaries} \\ 1 & \text{in fluid regions.} \end{cases} \quad (6)$$

Let us consider confining the bacterial suspensions in a closed circular domain. To represent the circular domain whose radius is R and center is at the origin, the three regions are defined as follows:

$$\begin{aligned} r < R - \delta &: \text{fluid,} \\ R - \delta \leq r \leq R + \delta &: \text{boundary,} \\ r > R + \delta &: \text{solid,} \end{aligned} \quad (7)$$

where 2δ is the thickness of the smoothed boundary and r is the distance from the origin. There are several candidates satisfying the above condition [Eqs. (6) and (7)]. Let us adopt the seemingly simplest one,

$$\phi(r) = \frac{1}{2} \tanh \frac{R-r}{d} + \frac{1}{2}, \quad (8)$$

where the thickness of the fluid-solid boundary is order d . Note that the smoothed profile Eq. (8) is not exactly equal to 0/1 in the solid (fluid) regions and we introduce a cutoff to divide the three regions (see Sec. III C for details).

Using this smoothed profile ϕ , we modify the integrals in the functional $\mathcal{F}[\mathbf{v}]$ [Eq. (5)] as follows:

$$\int_V d\mathbf{r} \rightarrow \int d\mathbf{r}\phi, \quad (9)$$

$$\int_S dS \rightarrow \int d\mathbf{r}|\nabla\phi|, \quad (10)$$

where the integral $\int d\mathbf{r}$ is taken over the whole (fluid, solid and their boundary) regions.

Equation (5) is now rewritten as

$$\begin{aligned} \mathcal{F}_\phi[\mathbf{v}] = & \int d\mathbf{r}\phi \left\{ -q\partial_i v_i + \frac{\alpha}{2}v_i v_i + \frac{\beta}{4}v_i v_j v_j \right. \\ & \left. + \frac{\Gamma_0}{2}(\partial_j v_i)(\partial_j v_i) + \frac{\Gamma_2}{2}(\partial_j \partial_j v_i)(\partial_k \partial_k v_i) \right\} \\ & + \frac{\xi}{2} \int d\mathbf{r}|\nabla\phi|(\mathbf{n} \times \mathbf{v})_z^2. \end{aligned} \quad (11)$$

Using the above functional $\mathcal{F}_\phi[\mathbf{v}]$, the basic equation of our simulation is given by

$$\partial_t \mathbf{v} = -\frac{\delta \mathcal{F}_\phi[\mathbf{v}]}{\delta \mathbf{v}} - \lambda_0 \phi \mathbf{v} \cdot \nabla \mathbf{v}. \quad (12)$$

Note that ϕ is also put in the λ_0 term. The above replacements using the smoothed profile ϕ [i.e., Eqs. (9), (10), and the λ_0 term in Eq. (12)] will be justified in Sec. III B and Appendix A.

B. The limit boundary thickness $\rightarrow 0$

Let us identify the forms of our modified TTSH equation [Eq. (12)] in each (solid, fluid, and boundary) region in the limit of $d \rightarrow 0$. We show here only the outline of the calculation and the results. For the details, see Appendix A.

In the limit $d \rightarrow 0$, $\phi(\mathbf{r}) \rightarrow \Theta(R-r)$ and $\nabla\phi \rightarrow -\delta(r-R)\mathbf{n}$, where $\Theta(\cdot)$ is the step function and $\delta(\cdot)$ is the delta function. In the fluid region, Eq. (12) reduces to the TTSH equation with no boundary [Eq. (1)]. In the solid region, Eq. (12) gives

$$\partial_t \mathbf{v} = 0. \quad (13)$$

Hence, by giving the initial condition where $\mathbf{v} = 0$ in the solid region, $\mathbf{v} = 0$ is satisfied in the subsequent time steps.

At the fluid-solid boundary, we obtain

$$-\xi(\mathbf{n} \times \mathbf{v})_z = \left\{ \mathbf{n} \times \left(\overset{\leftrightarrow}{\sigma} \cdot \mathbf{n} - \Gamma_2 \frac{1}{R} \nabla^2 \mathbf{v} \right) \right\}_z, \quad (14)$$

where $\overset{\leftrightarrow}{\sigma}$ is the stress tensor of the TTSH equation defined by

$$\partial_i v_i = \partial_j \sigma_{ij} - (\alpha + \beta v_j v_j) v_i, \quad (15)$$

$$\sigma_{ij} \equiv -q\delta_{ij} - \lambda_0 v_i v_j + \Gamma_0 \partial_j v_i - \Gamma_2 \partial_j \partial_k \partial_k v_i. \quad (16)$$

Equation (14) is the Navier slip boundary condition $(-\xi(\mathbf{n} \times \mathbf{v})_z = [\mathbf{n} \times (\overset{\leftrightarrow}{\sigma} \cdot \mathbf{n})]_z)$ with a correction term $[-(\Gamma_2/R)(\mathbf{n} \times \nabla^2 \mathbf{v})_z]$. For more details on the Navier slip boundary condition, see, e.g., Ref. [27]. The Navier slip boundary condition states that the tangential component of the velocity at the boundary is proportional to the tangential component of the stress and has been used not only for Navier-Stokes fluids but also for several active systems [21,28].

TABLE I. Fixed parameters through all the simulations. $v_0 = \sqrt{|\alpha|/\beta}$ and $\Lambda_0 = 2\pi\sqrt{2\Gamma_2/|\Gamma_0|}$.

J	256
K	85
$\alpha/(v_0/\Lambda_0)$	-0.27
$\beta/(1/(v_0\Lambda_0))$	0.27
$\Gamma_0/(v_0\Lambda_0)$	-0.078
$\Gamma_2/(v_0\Lambda_0^3)$	0.00099
d/Λ_0	0.31

C. Remarks on the simulation techniques

Let us comment on the practical techniques to calculate Eq. (12). In our numerical simulations, Eq. (12) is rewritten in terms of the stream function ψ , defined by $v_i = \epsilon_{ij}\partial_j\psi$, where ϵ_{ij} is the two-dimensional Levi-Civita symbol, defined by $\epsilon_{xy} = -\epsilon_{yx} = 1$, $\epsilon_{xx} = \epsilon_{yy} = 0$ (for details, see Appendix B). By introducing ψ , the incompressibility, Eq. (2), is automatically satisfied and there is no need to solve the Poisson equation for the Lagrange multiplier q . From the stream function ψ , we can calculate the velocity $v_i (= \epsilon_{ij}\partial_j\psi)$, the vorticity $\omega (= -\nabla^2\psi)$, and their spatial derivatives.

We use a pseudospectral method and the fourth order Runge-Kutta formula for the discretization in space and time, respectively [29]. The cutoff wave number K of the Fourier expansion is chosen to satisfy the 3/2 rule for K and the number of lattice points in each direction J : $J \geq 3K + 1$ (see Table I).

The initial velocity field is random in the region $r < 0.7R$ and 0 in the region $r > 0.7R$.

As already mentioned in Sec. III A, we introduce a cutoff to divide the three (solid, fluid, and boundary) regions as follows:

$$r < R - 1.5d : \text{fluid},$$

$$R - 1.5d < r < R + 1.5d : \text{boundary},$$

$$R + 1.5d < r : \text{solid}, \quad (17)$$

where r , R , and d are the same as in Eq. (8).

To satisfy the impermeability $\mathbf{n} \cdot \mathbf{v} = 0$ at boundaries and $\mathbf{v} = 0$ in the solid regions, we set the normal component of the velocity at the boundary and the velocity in the solid region to zero at each time step.

In Sec. IV, all physical quantities are nondimensionalized using the characteristic speed of bacteria v_0 and the characteristic length of spacial pattern Λ_0 . The nondimensionalized values of the fixed parameters through all the simulations are presented in Table I.

IV. RESULTS AND DISCUSSION

A. Vorticity and velocity profiles and oscillation of edge current

Using the simulation method explained in Sec. III, we successfully realized the edge current. Figures 1 and 2 are typical snapshots of the vorticity and velocity fields, respectively. See Ref. [30] for the time evolution of the vorticity and velocity fields. We can observe turbulence-like behavior in the bulk regions and unidirectional flow (edge current) at the boundary. Focusing on the boundary region in Fig. 2, we find the emergence of a counter-rotating double layer which is

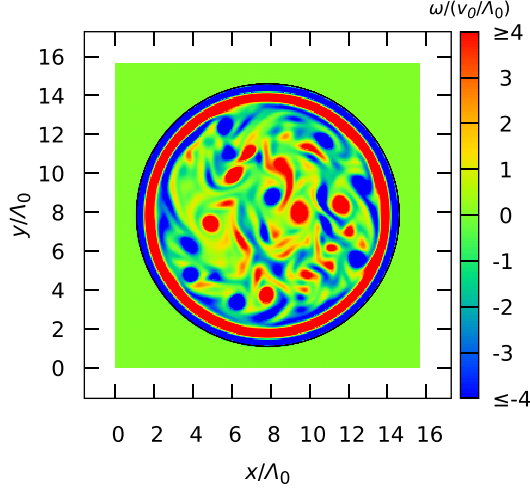


FIG. 1. A typical simulation snapshot of the vorticity field $\omega/(v_0/\Lambda_0) = (\nabla \times \mathbf{v})_z/(v_0/\Lambda_0)$ at the time $t/(\Lambda_0/v_0) = 235.2$. Parameters other than those in Table I are as follows: time increment $h/(\Lambda_0/v_0) = 0.000555$, $\lambda_0 = 6.0$, $R/\Lambda_0 = 6.3$, and $\xi/v_0 = 2.8 \times 10^{-2}$. The black line indicates the outer edge of the smoothed boundary.

reminiscent of the one reported in the experiment of Wioland *et al.* [24]. The emergence of this counter-rotating double layer in our simulations can be explained as follows: The TTSH equation has a characteristic length scale Λ_0 determined by its Γ terms and the direction of the velocity field switches over the distance $\sim \Lambda_0$. Thus, if clockwise (counterclockwise) edge current emerges at the boundary, respectively, counterclockwise (clockwise) flow emerges inside, leaving the distance $\sim \Lambda_0$ from the outer counter-rotating layer. The inner turbulent flow appears to destroy further counter-rotating layers that would be expected to emerge from the same argument, leaving only the double layers in our simulations.

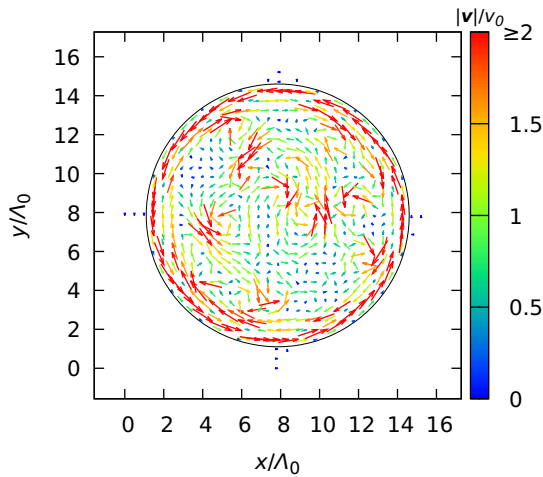


FIG. 2. A typical simulation snapshot of the velocity field \mathbf{v}/v_0 at the time $t/(\Lambda_0/v_0) = 235.2$. Parameters other than those in Table I are the same as in Fig. 1. The black line indicates the outer edge of the smoothed boundary. Velocity arrows are drawn at intervals of eight lattice points in each direction.

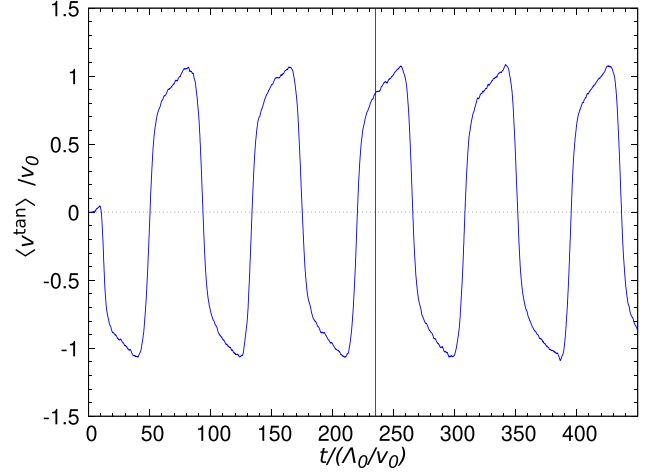


FIG. 3. A typical example of the time evolution of $\langle v^{\text{tan}} \rangle$. Parameters other than those in Table I are the same as in Fig. 1. The vertical red line indicates the time at which the snapshots (Figs. 1 and 2) are obtained.

Now let us comment on the relevant length scales in the experiment of Wioland *et al.* [24]. The thickness of the boundary layer ($\sim 4 \mu\text{m}$) has almost the same value as the length of each single bacterium ($\sim 5 \mu\text{m}$) and they argue that the bacteria trapped in the outer layer generate the backflow and it stabilizes the opposite-directional bulk flow. Here, recall that, as already mentioned in Sec. I, the typical vortex size of bacterial turbulence (=the spacing between counter-rotating double layers in our simulations) is larger than the length of single bacterium. Therefore, the mechanisms of the emergence of the double layer in our simulations and the experiment by Wioland *et al.* are different.

To determine the direction of the edge current quantitatively, let us introduce the following quantity:

$$\langle v^{\text{tan}} \rangle \equiv \frac{1}{N_b} \sum_{i \in \text{boundary}} v^{\text{tan}}(i), \quad (18)$$

where $v^{\text{tan}} (= (\mathbf{n} \times \mathbf{v})_z)$ is the tangential component of the velocity at the boundary, i is the lattice label, the summation $\sum_{i \in \text{boundary}}$ is taken over the lattice points in the boundary region defined by Eq. (17), and N_b is the total number of lattice points in the boundary region. $\langle v^{\text{tan}} \rangle > 0$ and < 0 corresponds to the counterclockwise and clockwise edge current, respectively.

An example of the time evolution of $\langle v^{\text{tan}} \rangle$ is shown in Fig. 3, which demonstrates that the sign of $\langle v^{\text{tan}} \rangle$ periodically changes. This means that the direction of the edge current temporally oscillates.

B. What causes the oscillation?

Here, one simple question arises: What causes the oscillation? To be more specific, which term in the TTSH equation causes the oscillation? To answer this question, let us focus on the functional-derivative form of the TTSH equation (Eq. (3) with the functional \mathcal{F} [Eq. (5)]:

$$\partial_t \mathbf{v} = -\frac{\delta \mathcal{F}}{\delta \mathbf{v}} - \lambda_0 \mathbf{v} \cdot \nabla \mathbf{v}. \quad (19)$$

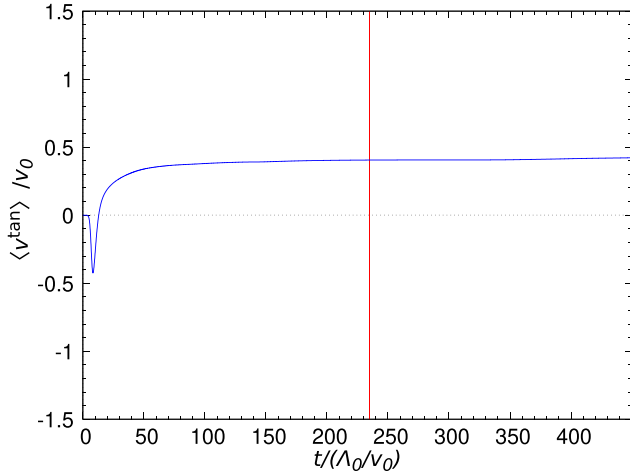


FIG. 4. A typical example of the time evolution of $\langle v^{\text{tan}} \rangle$ for $\lambda_0 = 0$. Parameters other than those in Table I are the same as in Fig. 1 except the value of λ_0 . The vertical red line indicates the time at which the snapshots (Figs. 5 and 6) are obtained.

Without the λ_0 term, Eq. (19) would become $\partial_t \mathbf{v} = -\delta \mathcal{F} / \delta \mathbf{v}$ and the velocity field would settle in a stationary state which minimizes the functional \mathcal{F} . Thus, oscillatory behavior is not expected to occur without the λ_0 term. Figures 4–6 show the results of simulation with $\lambda_0 = 0$ and we can confirm that oscillation does not occur. Therefore, we should attribute the temporal oscillation to the λ_0 term. The oscillation occurs for small but finite λ_0 , and the discussion on the threshold value is given in Appendix D. Here, let us give several comments on the vorticity and velocity field for $\lambda_0 = 0$: Looking at the vorticity field (Fig. 5), we can observe the vortices whose linear size rescaled by Λ_0 is order ~ 1 . In the velocity field (Fig. 6), the magnitude of the velocity rescaled by v_0 is order

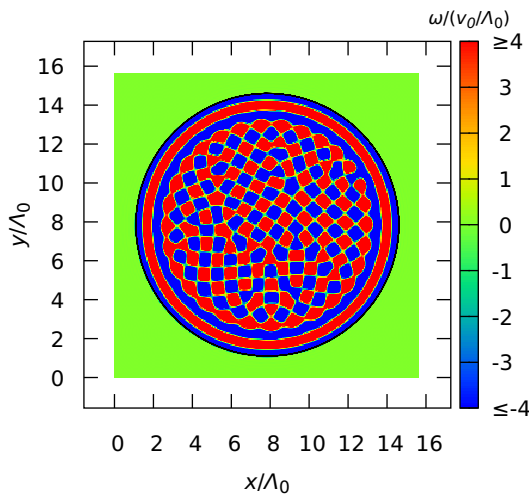


FIG. 5. A typical simulation snapshot of the vorticity field $\omega / (v_0 / \Lambda_0) = (\nabla \times \mathbf{v})_z / (v_0 / \Lambda_0)$ for $\lambda_0 = 0$ at the time $t / (\Lambda_0 / v_0) = 235.2$. Parameters other than those in Table I are the same as in Fig. 1 except the value of λ_0 . The black line indicates the outer edge of the smoothed boundary. In the bulk region, we can observe the stationary vortex lattice which has been observed in Ref. [31].

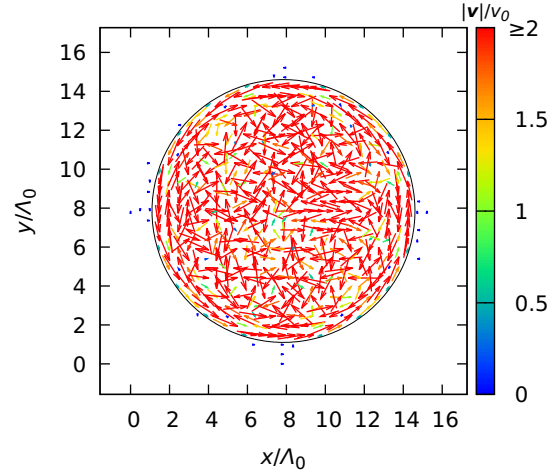


FIG. 6. A typical simulation snapshot of the velocity field \mathbf{v} / v_0 for $\lambda_0 = 0$ at the time $t / (\Lambda_0 / v_0) = 235.2$. Parameters other than those in Table I are the same as in Fig. 1 except the value of λ_0 . The black line indicates the outer edge of the smoothed boundary. Velocity arrows are drawn at intervals of eight lattice points in each direction.

~ 1 . Note that Λ_0 and v_0 are determined, respectively, by the Γ terms and α , β term in \mathcal{F} . From the above discussions, we can confirm that, without the λ_0 term, the result profiles become ones which minimize the functional \mathcal{F} .

Next we give a simple argument on how the λ_0 term causes the oscillation: The velocity field at the boundary and the inner counter-rotating layer can be approximately written by $\mathbf{v} \sim c(r) \mathbf{e}_\theta$, where \mathbf{e}_θ is the azimuthal unit vector of two-dimensional polar coordinate whose origin is at the center of the circular domain. Using this \mathbf{v} , we can calculate the advection term $-\lambda_0 \mathbf{v} \cdot \nabla \mathbf{v}$ and obtain

$$-\lambda_0 \mathbf{v} \cdot \nabla \mathbf{v} \sim \frac{\lambda_0 \{c(r)\}^2}{R} \mathbf{e}_r, \quad (20)$$

where \mathbf{e}_r is the radial unit vector of the two-dimensional polar coordinate. Therefore, the advection term has an outward radial profile regardless of the sign of $c(r)$ (i.e., the direction of the flow) (see Fig. 7) and this term will exert the velocity field to rotate toward the opposite direction. Here, note that the outer flow never has a radial component because of the boundary condition and then it cannot rotate. However, the

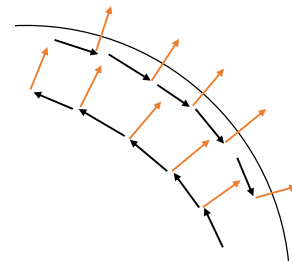


FIG. 7. A schematic of the velocity \mathbf{v} (black arrow) and the advection term $-\lambda_0 \mathbf{v} \cdot \nabla \mathbf{v}$ (orange arrow) at the boundary. The curved black line indicates the outer edge of the smoothed boundary.

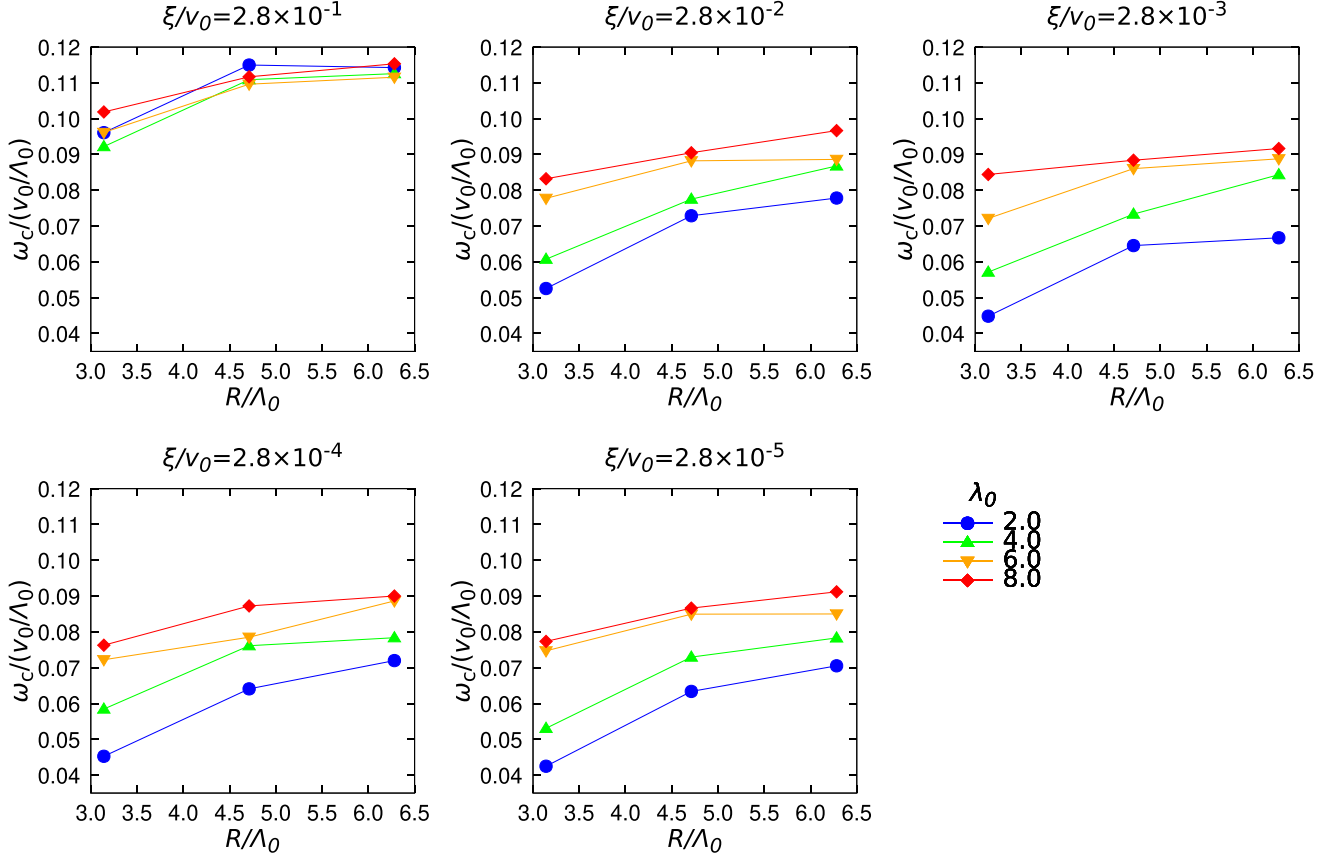


FIG. 8. The radius of the fluid region R versus the characteristic angular frequency ω_c for G1 geometry. All simulations are performed with $h/(\Lambda_0/v_0) = 0.000555$ and parameters listed in Table I.

inner counter-rotating flow can have a radial component and then it can rotate and switch its direction.

C. Oscillation frequency vs R , ξ , and λ_0

Next, let us investigate the relations between the behavior of the edge current oscillation and the parameters R , ξ , and λ_0 , with particular focus on the oscillation frequency. To characterize the oscillation frequency, let us introduce the characteristic angular frequency ω_c defined by

$$\omega_c \equiv \frac{\sum_n |\text{FT}[\langle v^{\text{tan}} \rangle]_n|^2 \omega_n}{\sum_n |\text{FT}[\langle v^{\text{tan}} \rangle]_n|^2}, \quad (21)$$

where $\text{FT}[\langle v^{\text{tan}} \rangle]_n$ is the n th component of the Fourier transform of $\langle v^{\text{tan}} \rangle$ and ω_n is the angular frequency of the n th Fourier mode.

We performed simulations with all combinations of the following R , ξ , and λ_0 : $R/\Lambda_0 = 1.0, 1.6, 3.1, 4.7, 6.3$, $\xi/v_0 = 2.8 \times 10^{-1}, 2.8 \times 10^{-2}, 2.8 \times 10^{-3}, 2.8 \times 10^{-4}, 2.8 \times 10^{-5}$, and $\lambda_0 = 0, 2.0, 4.0, 6.0, 8.0$. The results are shown in Figs. 8 and 9. When $\lambda_0 = 0$ or $R/\Lambda_0 = 1.0, 1.6$, the oscillation of $\langle v^{\text{tan}} \rangle$ does not occur as in Fig. 4 and then we do not plot them in Figs. 8 and 9. We can observe that ω_c tends to increase with increase of λ_0 , R , and ξ . Here, let us comment on the dependence on ξ . ω_c tends to increase with ξ , but is almost constant in the small- ξ region. This is probably because, at $\xi/v_0 \sim 10^{-2}$, the boundary condition has already reduced to the free-slip one. (Recall the discussion presented in Sec. II:

In the limit $\xi \rightarrow 0$, the boundary condition will reduce to the stress-free slip condition.)

Here, note that the larger the advection strength λ_0 is, the more excited the turbulent behavior in the bulk become. Furthermore, the larger the drag coefficient ξ is, the more subject to the bulk turbulence the edge current is. From the above arguments, we can say that the edge current oscillation will be related to the turbulent behavior in the bulk region. The relations between ω_c and R will be discussed after the simulations in two more geometries in Sec. IV D.

D. Other geometries

The next question is whether the edge current oscillation occurs in other geometries. To answer this question, we have performed the simulations in two more geometries. Let us call the geometry used in Figs. 1–6 G1. The first one of the two new geometries (hereinafter called G2, see Figs. 10 and 11) is the case where the solid and fluid regions are swapped in G1. The second one (hereinafter called G3, see Figs. 13 and 14) is the case where the active fluid is sandwiched by two parallel straight walls perpendicular to the x axis and periodic boundary condition is imposed in the y direction.

We can implement the above two new geometries, G2 and G3, only by replacing the smoothed profile ϕ [Eq. (8)] of G1. This is an advantage of the SPM.

The smoothed profile for G2, $\tilde{\phi}$, is

$$\tilde{\phi} = 1 - \phi = \frac{1}{2} - \frac{1}{2} \tanh \frac{R-r}{d}, \quad (22)$$

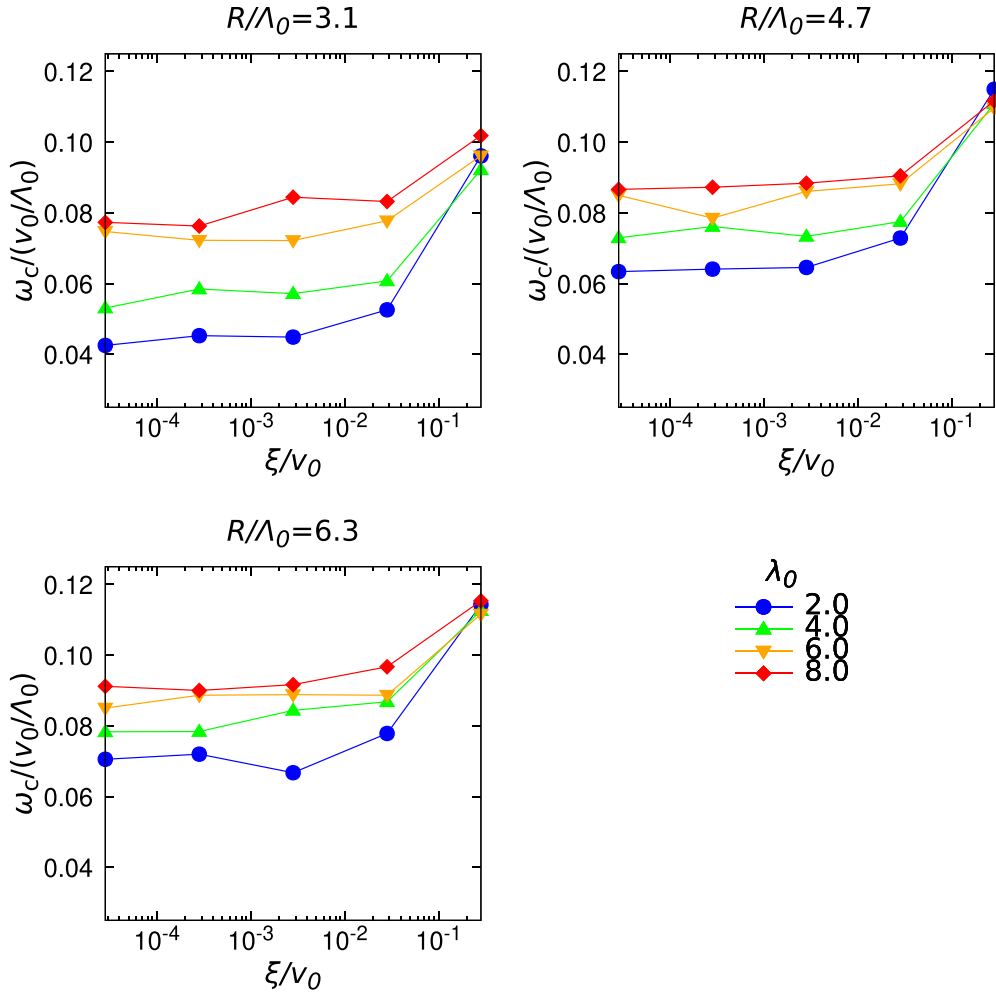


FIG. 9. The drag coefficient ξ versus the characteristic angular frequency ω_c for G1 geometry. All simulations are performed with $h/(\Lambda_0/v_0) = 0.000555$ and parameters listed in Table I.

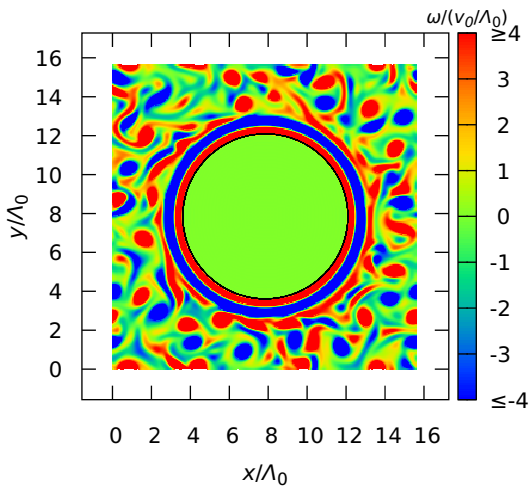


FIG. 10. A typical simulation snapshot of the vorticity field $\omega/(v_0/\Lambda_0) = (\nabla \times \mathbf{v})_z/(v_0/\Lambda_0)$ at the time $t/(\Lambda_0/v_0) = 312.9$ for G2 geometry. Parameters other than those in Table I are as follows: time increment $h/(\Lambda_0/v_0) = 0.000370$, $\lambda_0 = 4.0$, $R/\Lambda_0 = 4.7$, and $\xi/v_0 = 2.8 \times 10^{-2}$. The black line indicates the outer edge of the smoothed boundary.

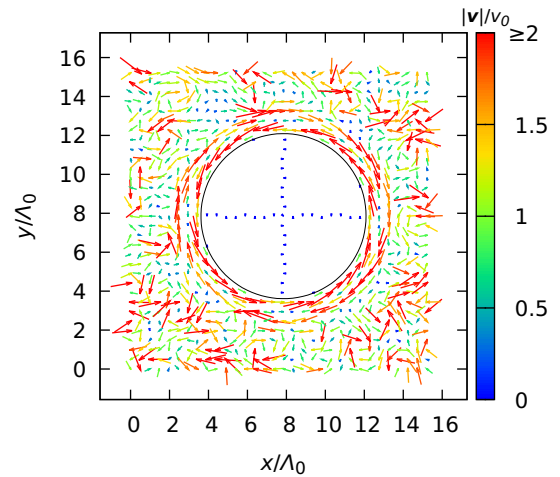


FIG. 11. A typical simulation snapshot of the velocity field \mathbf{v}/v_0 at the time $t/(\Lambda_0/v_0) = 312.9$ for G2 geometry. Parameters other than those in Table I are the same as in Fig. 10. The black line indicates the outer edge of the smoothed boundary. Velocity arrows are drawn at intervals of eight lattice points in each direction.

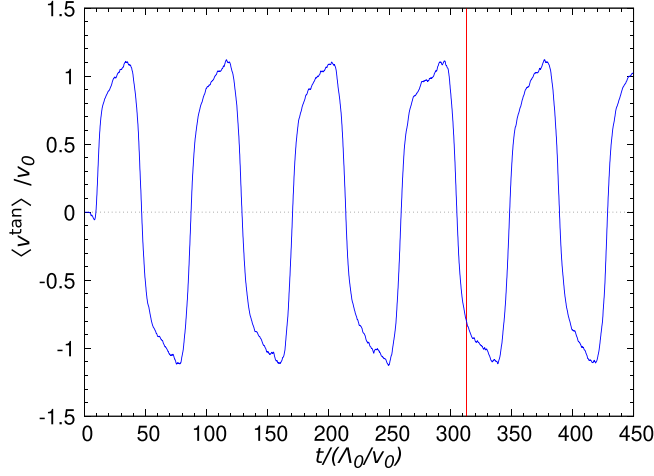


FIG. 12. A typical example of the time evolution of $\langle v^{\text{tan}} \rangle$ for G2 geometry. Parameters other than those in Table I are the same as in Fig. 10. The vertical red line indicates the time at which the snapshots (Figs. 10 and 11) are obtained.

where R is the radius of the circular solid domain and r, d are the same ones already used in Eq. (8). The smoothed profile for G3, $\tilde{\phi}$, can be made by replacing r in ϕ by x ,

$$\tilde{\phi} = \frac{1}{2} \tanh \frac{R-x}{d} + \frac{1}{2}, \quad (23)$$

where $2R$ is the spacing of the two walls and d is the same as in Eq. (8).

In Figs. 10, 11, 13, and 14, we can observe that the edge current emerges again in G2 and G3. Furthermore, Figs. 12 and 15 show that the edge current oscillation also occurs also in G2 and G3. See Ref. [30] for the time evolution of the vorticity and velocity field. G3 geometry is also the subject of previous studies [32,33], and their results are compared with ours in Appendix E. Here, let us comment on what causes the

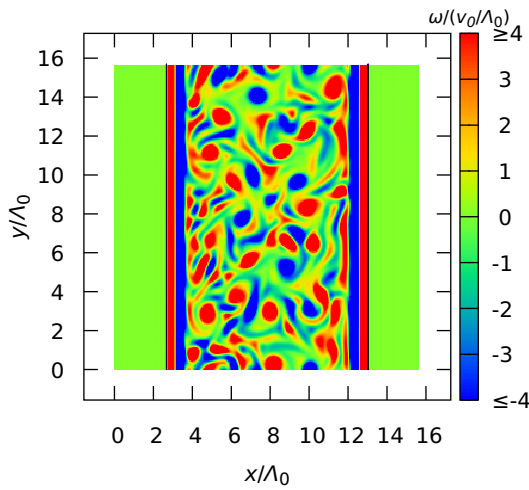


FIG. 13. A typical simulation snapshot of the vorticity field $\omega / (v_0 / \Lambda_0) = (\nabla \times \mathbf{v})_z / (v_0 / \Lambda_0)$ at the time $t / (\Lambda_0 / v_0) = 274.6$ for G3 geometry. Parameters other than those in Table I are as follows: time increment $h / (\Lambda_0 / v_0) = 0.000370$, $\lambda_0 = 4.0$, $R / \Lambda_0 = 4.7$, and $\xi / v_0 = 2.8 \times 10^{-2}$. Note that the spacing of two walls is $2R / \Lambda_0$. The black line indicates the outer edge of the smoothed boundary.

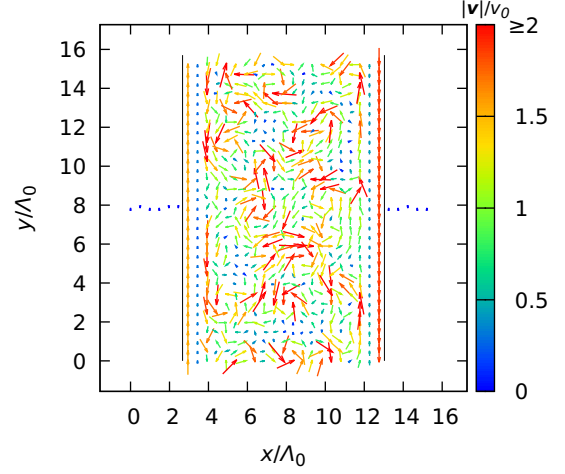


FIG. 14. A typical simulation snapshot of the velocity field \mathbf{v} / v_0 at the time $t / (\Lambda_0 / v_0) = 274.6$ for G3 geometry. Parameters other than those in Table I are the same as in Fig. 13. The black line indicates the outer edge of the smoothed boundary. Velocity arrows are drawn at intervals of eight lattice points in each direction.

oscillation. In the case of G2, we can apply the same argument as in Sec. IV B. In the geometry G3, applying the similar argument as in Sec. IV B, we obtain the result $-\lambda_0 \mathbf{v} \cdot \nabla \mathbf{v} \sim 0$ as follows: The velocity at the boundary and inner counter-rotating layer can be approximately written by $\mathbf{v} \sim c(x)\mathbf{e}_y$ and $-\lambda_0 \mathbf{v} \cdot \nabla \mathbf{v} \sim -\lambda_0 c(x) \partial / \partial y (c(x)\mathbf{e}_y) = 0$. However, in the inner counter-rotating layer, the velocity is affected by the inner turbulent flow and distorted. Therefore, the inner layer locally has finite curvature and then we can apply the same argument as in Sec. IV B locally.

Next, we calculate the characteristic angular frequency ω_c and investigate the relation between ω_c and R, ξ, λ_0 for G2 (Figs. 16 and 17) and G3 (Figs. 18 and 19). The values of R, ξ , and λ_0 are the same as in G1. In both geometries, as expected, for $\lambda_0 = 0$ edge current oscillation does not occur.

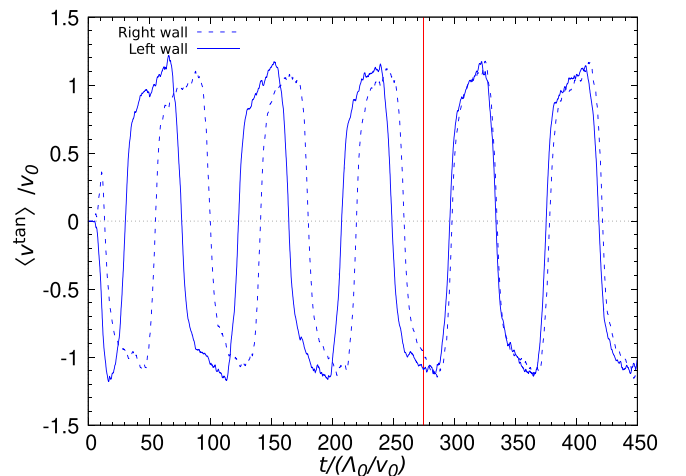


FIG. 15. A typical example of the time evolution of $\langle v^{\text{tan}} \rangle$ for G3 geometry. Parameters other than those in Table I are the same as in Fig. 13. The vertical red line indicates the time at which the snapshots (Figs. 13 and 14) are obtained.

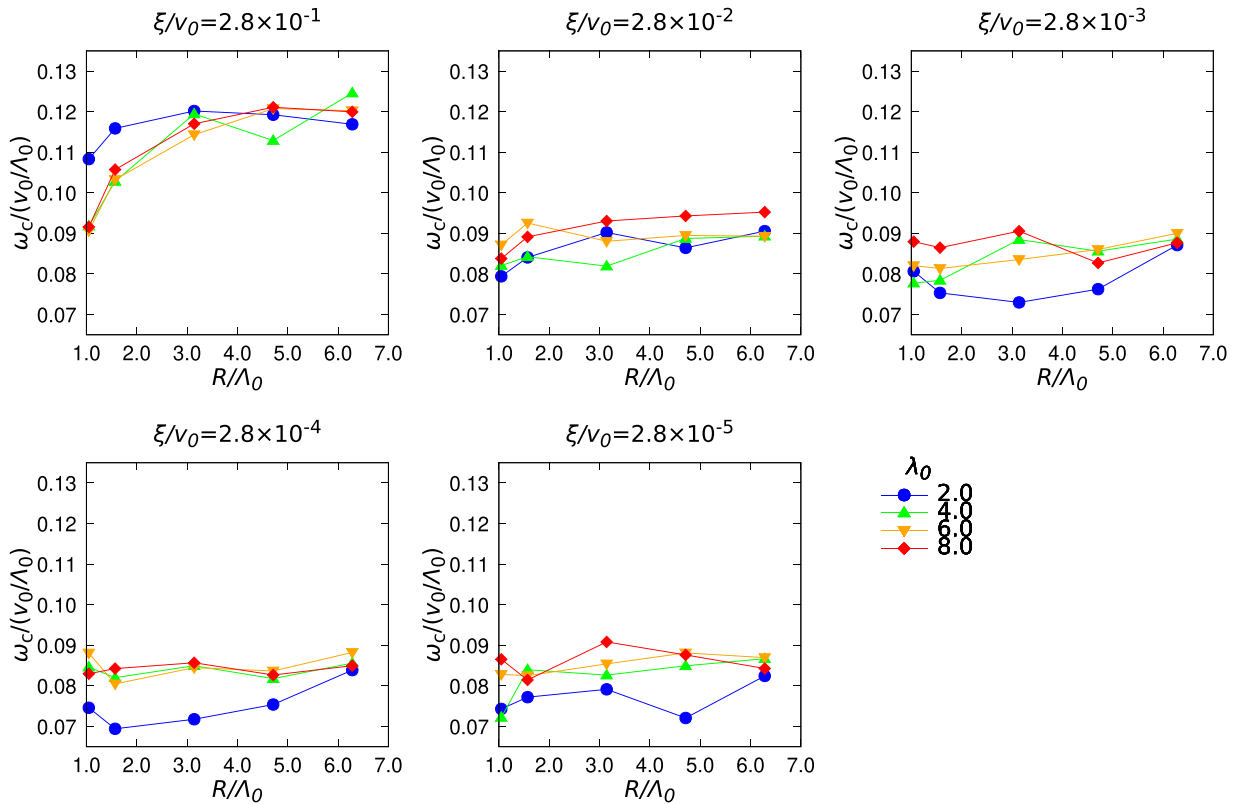


FIG. 16. The radius of the fluid region R versus the characteristic angular frequency ω_c for G2 geometry. All simulations are performed with $h/(\Lambda_0/v_0) = 0.000370$ and parameters listed in Table I.

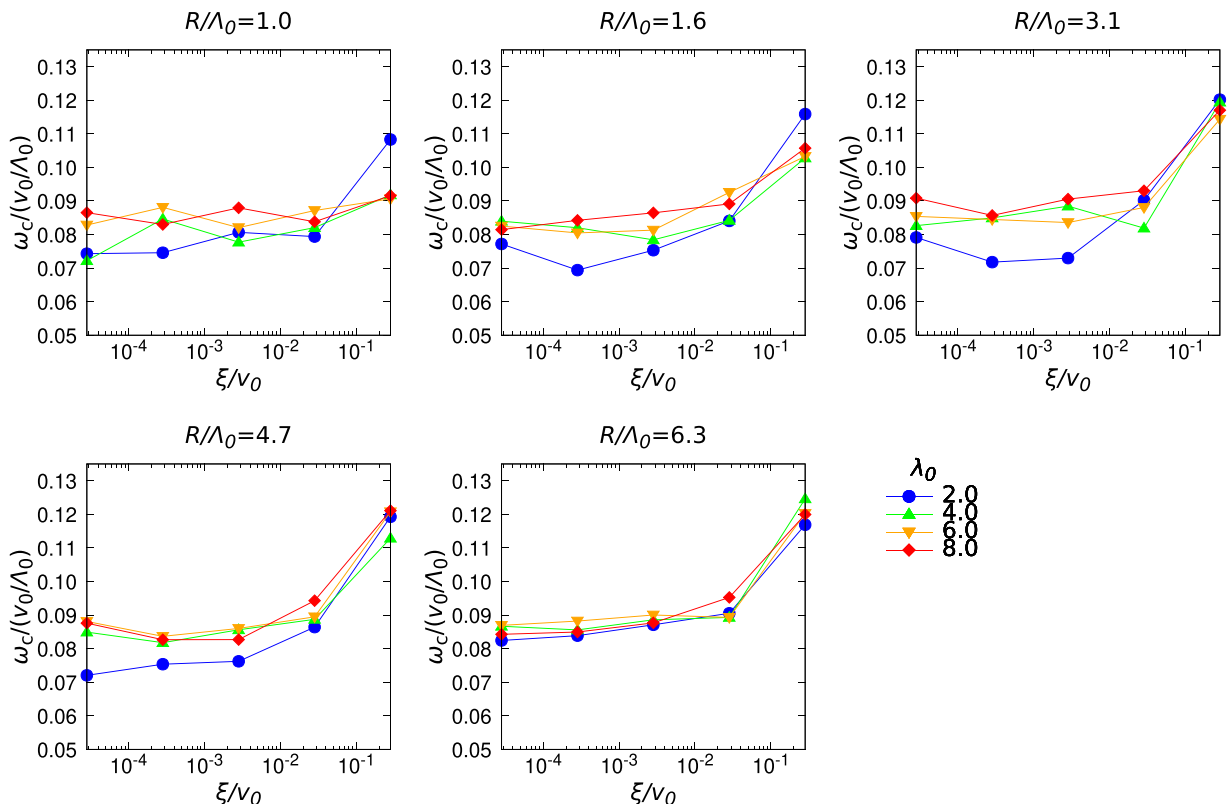


FIG. 17. The drag coefficient ξ versus the characteristic angular frequency ω_c for G2 geometry. All simulations are performed with $h/(\Lambda_0/v_0) = 0.000370$ and parameters listed in Table I.

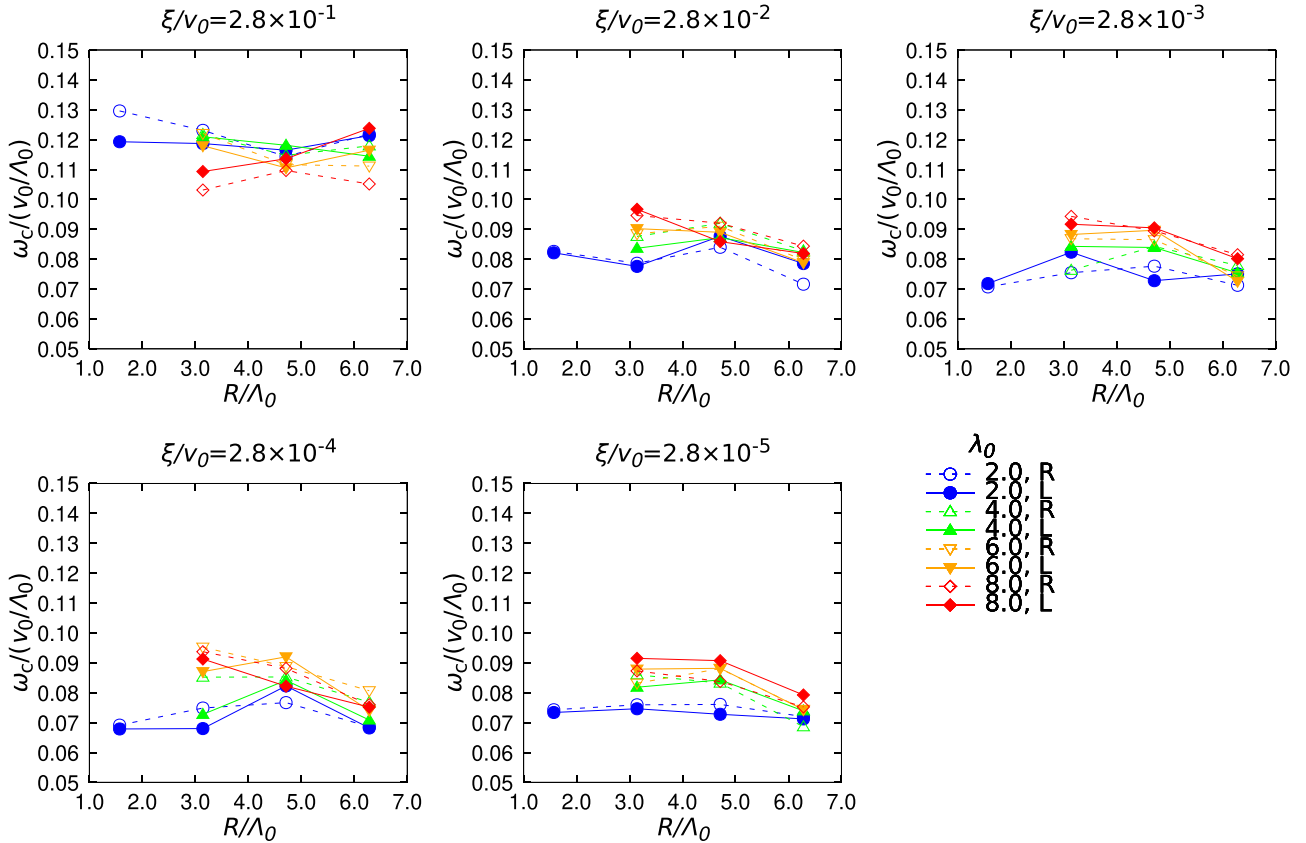


FIG. 18. Half of the spacing of two walls R versus the characteristic angular frequency ω_c for G3 geometry. ω_c is calculated in each (right and left) wall. R and L in the legend indicates the right and left wall, respectively. All simulations are performed with $h/(\Lambda_0/v_0) = 0.000370$ and parameters listed in Table I.

Unlike in the case of G1, in G2 geometry, oscillations occur for all R 's. In G3 geometry, for $R/\Lambda_0 = 1.0$ oscillation does not occur, for $R/\Lambda_0 = 1.6$ oscillation is observed only when $\lambda_0 = 2.0$ and for other R 's oscillation occurs for all values of λ_0 . As in the case of G1, we plot ω_c only for the cases where oscillation is observed. The dependence of ω_c on ξ for G2 and G3 is similar to that for G1 (see Figs. 17 and 19). However, the dependence on R and λ_0 looks different from the one for G1 geometry. First, let us comment on the relations between ω_c and λ_0 . In G3 geometry (Fig. 18 or 19), ω_c tends to increase slightly with the increase of λ_0 but the tendency is not so clear as in G1 geometry. In G2 geometry (Fig. 16 or 17), ω_c is insensitive to the variation of λ_0 . From the relations between ω_c and λ_0 in the three geometries, we can say that the more strongly confined the active fluids are, the greater effect the λ_0 -term has on the edge current oscillation. Next, let us mention the relations between ω_c and R . In G2 geometry (Fig. 16), ω_c is almost constant. In G3 geometry (Fig. 18), ω_c tends to decrease slightly with R . The typical value of ω_c for G3 is $\sim 0.08v_0/\Lambda_0$ (Fig. 18), close to the asymptotic value for G1 with large R . This is natural from the fact that the $R \rightarrow \infty$ limit of the G1 geometry can be regarded as the flat geometry G3. Furthermore, the typical value of ω_c for G2 is close to the one for G3. Those behaviors of ω_c in response to the variation of R suggests that the curvature of the boundary, when positive and small enough (large- R region in G1) or negative (G2), does not play an important role in the

oscillation of the edge current. Finally, ω_c 's tendency in G3 to slightly decrease with the increasing of R can be explained as follows: In G3 geometry, the smaller R is, the more narrow the region the active fluids are confined in, and then the more excited the turbulent behavior becomes. Therefore, ω_c become larger for smaller R .

V. CONCLUSION

The previous works on TTSH simulations seem to be insufficient in that, although the importance of edge current in bacterial dynamics has been reported in several experimental studies, the previous TTSH simulations adopted a non-slip boundary condition and did not describe such bacterial motions.

In this paper, we focused on the bacterial behavior at the fluid-solid boundary and adopted a slip boundary condition to investigate the effect of the boundary condition on the bacterial dynamics. To implement the slip boundary condition, we proposed an extended TTSH model, where a surface term which can be regarded as an energetic penalty for the tangential component of velocity is added to the functional in the TTSH equation. Furthermore, we applied the smoothed profile method to our model and performed numerical simulations in three boundary geometries. Our extended TTSH model successfully realized the edge current in three different boundary geometries. Furthermore, we unexpectedly

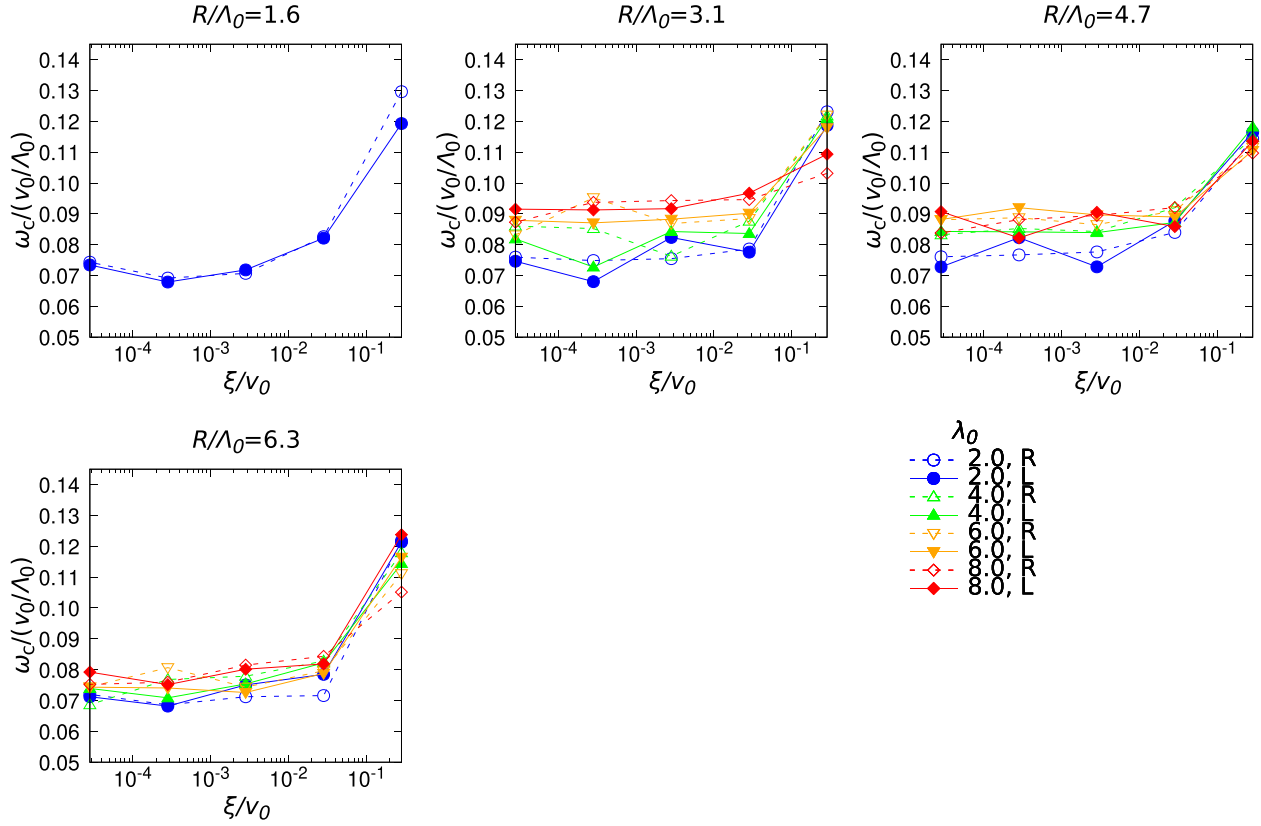


FIG. 19. The drag coefficient ξ versus the characteristic angular frequency ω_c for G3 geometry. ω_c is calculated in each (right and left) wall. R and L in the legend indicates the right and left wall, respectively. All simulations are performed with $h/(\Lambda_0/v_0) = 0.000370$ and parameters listed in Table I.

discovered the temporal oscillation of the direction of the edge current. The edge current oscillation is observed in all three boundary geometries. By a simple argument based on the functional-derivative form of the TTSH equation, the origin of the oscillation was identified as the λ_0 term (advection term) in the TTSH equation. Note that our argument identifies only the cause of the oscillation and its detailed mechanism is still an open question.

To determine the direction of the edge current, we introduced $\langle v^{\text{tan}} \rangle$, the average of the tangential component of the velocity in boundary regions, and we traced its time evolution. To characterize the oscillation of $\langle v^{\text{tan}} \rangle$ quantitatively, we calculate the power spectrum of the time evolution of $\langle v^{\text{tan}} \rangle$ and then the characteristic angular frequency ω_c . We investigated the dependence of ω_c on three parameters R , ξ and λ_0 .

We revealed the behavior of bacterial turbulence in contact with a slip boundary and our work indicates that the boundary condition could play an important role in bacterial dynamics.

To our knowledge, oscillating edge current of active fluids has never been observed. In our simulations, only the velocity field in two dimensions is considered, and the factors not taken into account in our study, say, the third dimension, the spatial variation of the density, or other degrees of freedom, might suppress the oscillation. How the oscillation could be promoted or suppressed could be an interesting direction of future studies. We also hope that the oscillating edge current may be observed in a carefully performed future experiment.

ACKNOWLEDGMENTS

The authors thank Prof. Y. T. Maeda and Dr. K. Beppu for fruitful discussions. H.M. is supported by JST SPRING, Grant No. JPMJSP2136. J.-i.F. is supported by JSPS KAKENHI (Grant No. JP21H01049). A substantial part of the computation has been done using the facilities of the Supercomputer Center, the Institute for Solid State Physics, the University of Tokyo. This work was supported by the JSPS Core-to-Core Program, “Advanced core-to-core network for the physics of self-organizing active matter (Grant No. JPJSCCA20230002)”.

APPENDIX A: DETAILS OF THE CALCULATION IN SEC. III B

This Appendix is devoted to proving that in the limit $d \rightarrow 0$, our extended TTSH equation [Eq. (12) with $\mathcal{F}_\phi[\mathbf{v}]$ given by (11)] reduces to Eq. (1) in the fluid region, Eq. (14) at the fluid-solid boundary and Eq. (13) in the solid region.

Substituting Eq. (11) into Eq. (12) and executing the functional derivative, we obtain

$$\begin{aligned} \partial_t \mathbf{v} = & -(\nabla \phi)q - \phi \nabla q - \alpha \phi \mathbf{v} - \beta \phi |\mathbf{v}|^2 \mathbf{v} \\ & + \Gamma_0 (\nabla \phi) \cdot \nabla \mathbf{v} + \Gamma_0 \phi \nabla^2 \mathbf{v} - \Gamma_2 (\nabla^2 \phi) \nabla^2 \mathbf{v} \\ & - 2\Gamma_2 (\nabla \phi) \cdot \nabla \nabla^2 \mathbf{v} - \Gamma_2 \phi (\nabla^2)^2 \mathbf{v} \\ & - \xi |\nabla \phi|^{-1} ((\nabla \phi) \cdot \vec{\epsilon}) ((\nabla \phi) \times \mathbf{v})_z - \lambda_0 \phi \mathbf{v} \cdot \nabla \mathbf{v}, \end{aligned} \quad (\text{A1})$$

where $\vec{\epsilon}$ ($(\vec{\epsilon})_{ij} = \epsilon_{ij}$) is the two-dimensional Levi-Civita symbol, whose definition has already been given in Sec. III C.

As discussed in Ref. [26], in the limit $d \rightarrow 0$,

$$\phi(\mathbf{r}) \rightarrow \Theta(R-r) = \begin{cases} 1 & \text{for } r < R \\ 0 & \text{for } r > R \end{cases}, \quad (\text{A2})$$

$$\nabla\phi \rightarrow -\delta(r-R)\mathbf{n}, \quad (\text{A3})$$

$$|\nabla\phi| \rightarrow \delta(r-R), \quad (\text{A4})$$

$$\frac{\nabla\phi}{|\nabla\phi|} \rightarrow -\mathbf{n}. \quad (\text{A5})$$

Hence, in the limit $d \rightarrow 0$, Eq. (A1) becomes

$$\begin{aligned} \partial_t \mathbf{v} = & \Theta(R-r) \left\{ -\nabla q - (\alpha + \beta|\mathbf{v}|^2)\mathbf{v} + \Gamma_0 \nabla^2 \mathbf{v} - \Gamma_2 (\nabla^2)^2 \mathbf{v} \right. \\ & \left. - \lambda_0 \mathbf{v} \cdot \nabla \mathbf{v} \right\} + \delta(r-R) \left\{ \mathbf{n}q - \Gamma_0 \mathbf{n} \cdot \nabla \mathbf{v} \right. \\ & \left. + 2\Gamma_2 \mathbf{n} \cdot \nabla \nabla^2 \mathbf{v} - \xi(\mathbf{n} \cdot \vec{\epsilon})(\mathbf{n} \times \mathbf{v})_z \right\} \\ & + \Gamma_2 \{ \nabla \cdot (\delta(r-R)\mathbf{n}) \} \nabla^2 \mathbf{v}. \end{aligned} \quad (\text{A6})$$

In the fluid region ($r < R$), $\Theta(R-r) = 1$, $\delta(r-R) = 0$. Hence, Eq. (A6) reduces to the TTSH equation with no boundaries, Eq. (1). In the solid region ($r > R$), $\Theta(R-r) = 0$, $\delta(r-R) = 0$. Thus, Eq. (A6) reduces to

$$\partial_t \mathbf{v} = 0. \quad (\text{A7})$$

Therefore, by preparing the initial condition where $\mathbf{v} = 0$ in the solid region, $\mathbf{v} = 0$ is satisfied at the subsequent time steps. The equation at the fluid-solid boundary is obtained by integrating Eq. (A6) with respect to r from $R-\epsilon$ to $R+\epsilon$, where $\epsilon > 0$:

$$\begin{aligned} \int_{R-\epsilon}^{R+\epsilon} dr \partial_t \mathbf{v} = & \int_{R-\epsilon}^{R+\epsilon} dr \Theta(R-r) \left\{ -\nabla q - (\alpha + \beta|\mathbf{v}|^2)\mathbf{v} \right. \\ & \left. + \Gamma_0 \nabla^2 \mathbf{v} - \Gamma_2 (\nabla^2)^2 \mathbf{v} - \lambda_0 \mathbf{v} \cdot \nabla \mathbf{v} \right\} \\ & + \int_{R-\epsilon}^{R+\epsilon} dr \delta(r-R) \left\{ \mathbf{n}q - \Gamma_0 \mathbf{n} \cdot \nabla \mathbf{v} \right. \\ & \left. + 2\Gamma_2 \mathbf{n} \cdot \nabla \nabla^2 \mathbf{v} - \xi(\mathbf{n} \cdot \vec{\epsilon})(\mathbf{n} \times \mathbf{v})_z \right\} \\ & + \int_{R-\epsilon}^{R+\epsilon} dr \Gamma_2 \{ \nabla \cdot (\delta(r-R)\mathbf{n}) \} \nabla^2 \mathbf{v}. \end{aligned} \quad (\text{A8})$$

The left-hand side and the first term of the right-hand side of Eq. (A8), whose integrand has a finite value, go to zero as $\epsilon \rightarrow 0$. It is quite easy to execute the integral of the second term of the right-hand side. The third integral of the right-hand side can be evaluated as follows:

$$\begin{aligned} & \int_{R-\epsilon}^{R+\epsilon} dr \Gamma_2 \{ \nabla \cdot (\delta(r-R)\mathbf{n}) \} \nabla^2 \mathbf{v} \\ & = \int_{R-\epsilon}^{R+\epsilon} dr \Gamma_2 \left\{ \frac{1}{r} \frac{\partial}{\partial r} (r\delta(r-R)) \right\} \nabla^2 \mathbf{v} \\ & = \int_{R-\epsilon}^{R+\epsilon} dr \Gamma_2 \frac{\partial}{\partial r} \left\{ r\delta(r-R) \frac{1}{r} \nabla^2 \mathbf{v} \right\} \\ & \quad - \int_{R-\epsilon}^{R+\epsilon} dr \Gamma_2 r \delta(r-R) \frac{\partial}{\partial r} \left(\frac{1}{r} \nabla^2 \mathbf{v} \right) \end{aligned}$$

$$\begin{aligned} & = - \int_{R-\epsilon}^{R+\epsilon} dr \Gamma_2 \delta(r-R) \left\{ -\frac{1}{r} \nabla^2 \mathbf{v} + \frac{\partial}{\partial r} \nabla^2 \mathbf{v} \right\} \\ & = \Gamma_2 \frac{1}{R} \nabla^2 \mathbf{v} \Big|_{r=R} - \Gamma_2 \mathbf{n} \cdot \nabla \nabla^2 \mathbf{v} \Big|_{r=R}. \end{aligned} \quad (\text{A9})$$

Therefore, Eq. (A8) reduces to

$$\begin{aligned} 0 = & \mathbf{n}q - \Gamma_0 \mathbf{n} \cdot \nabla \mathbf{v} + \Gamma_2 \mathbf{n} \cdot \nabla \nabla^2 \mathbf{v} \\ & - \xi(\mathbf{n} \cdot \vec{\epsilon})(\mathbf{n} \times \mathbf{v})_z + \Gamma_2 \frac{1}{R} \nabla^2 \mathbf{v} \quad \text{for } r = R. \end{aligned} \quad (\text{A10})$$

To obtain the condition on the tangential component, taking the cross product of Eq. (A10) with \mathbf{n} , we obtain

$$-\xi(\mathbf{n} \times \mathbf{v})_z = \left[\mathbf{n} \times \left(\vec{\sigma} \cdot \mathbf{n} - \Gamma_2 \frac{1}{R} \nabla^2 \mathbf{v} \right) \right]_z \quad \text{for } r = R. \quad (\text{A11})$$

This is the Navier slip boundary condition with a correction term: $-(\Gamma_2/R)\mathbf{n} \times \nabla^2 \mathbf{v}$.

By taking the dot product of Eq. (A10) with \mathbf{n} , we can obtain one more boundary condition:

$$\begin{aligned} 0 = & q - \Gamma_0 \mathbf{n} \cdot \nabla(\mathbf{n} \cdot \mathbf{v}) \\ & + \Gamma_2 \mathbf{n} \cdot \nabla(\mathbf{n} \cdot \nabla^2 \mathbf{v}) + \Gamma_2 \frac{1}{R} \mathbf{n} \cdot \nabla^2 \mathbf{v} \quad \text{for } r = R. \end{aligned} \quad (\text{A12})$$

In the previous studies using the TTSH equation (Refs. [14, 15, 18]), the zero-vorticity boundary condition ($\omega = 0$) is imposed in addition to the zero-velocity condition ($\mathbf{v} = 0$). Equation (A12) can be regarded as a boundary condition for the derivatives of \mathbf{v} . Note that the zero-vorticity boundary condition, together with the zero velocity, also corresponds to imposing a boundary condition for the derivative of \mathbf{v} . Adding an appropriate surface term regarding the vorticity to the functional \mathcal{F} yields a boundary condition imposed directly on the vorticity. The introduction of such boundary conditions could be the subject of future study.

APPENDIX B: STREAM-FUNCTION REPRESENTATION OF THE TTSH EQUATION

In our calculations, the basic equation is rewritten in terms of the stream function ψ , defined by $v_i = \epsilon_{ij} \partial_j \psi$. Substituting $v_i = \epsilon_{ij} \partial_j \psi$ into Eq. (A1) and operating $\epsilon_{ik} \partial_k$ on both sides of the equation, we obtain the stream-function representation of the TTSH equation,

$$\begin{aligned} \partial_t \nabla^2 \psi = & -\alpha \{ (\nabla\phi) \cdot \nabla\psi - \phi\omega \} - \beta \{ (\nabla\phi) \cdot (\nabla\psi) \mathbf{v}^2 \\ & + 2\phi(\nabla\psi) \cdot (\nabla\mathbf{v}) \cdot \mathbf{v} - \phi\mathbf{v}^2\omega \} \\ & + \Gamma_0 \{ (\nabla\nabla\phi) : (\nabla\nabla\psi) - 2(\nabla\phi) \cdot \nabla\omega - \phi\nabla^2\omega \} \\ & + \Gamma_2 \{ (\nabla\nabla^2\phi) \cdot \nabla\omega + (\nabla^2\phi)(\nabla^2\omega) \\ & + 2(\nabla\nabla\phi) : (\nabla\nabla\omega) \\ & + 3(\nabla\phi) \cdot (\nabla\nabla^2\omega) + \phi(\nabla^2)^2\omega \} \\ & + \xi \{ |\nabla\phi|^{-3} (\nabla\phi) \cdot (\nabla\nabla\phi) \cdot (\nabla\phi)(\nabla\phi) \cdot \nabla\psi \\ & - |\nabla\phi|^{-1} (\nabla\phi) \cdot (\nabla\nabla\phi) \cdot \nabla\psi \\ & - |\nabla\phi|^{-1} (\nabla\phi) \cdot (\nabla\nabla\psi) \cdot \nabla\phi \end{aligned}$$

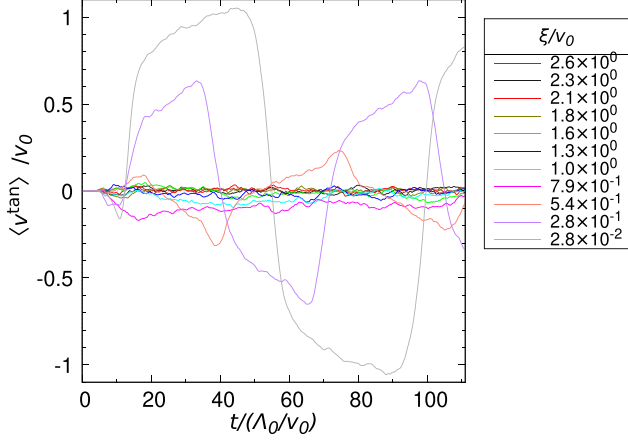


FIG. 20. Time evolution of $\langle v^{\text{tan}} \rangle$ for large values of ξ . Parameters other than those in Table I are as follows: $h/(\Lambda_0/v_0) = 0.000555$, $\lambda_0 = 4.0$, and $R/\Lambda_0 = 6.3$.

$$\begin{aligned}
 & - |\nabla\phi|^{-1}(\nabla^2\phi)(\nabla\phi) \cdot \nabla\psi \} \\
 & - \lambda_0\{(\nabla\phi) \cdot (\nabla\nabla\psi) \cdot \mathbf{v} \\
 & + \phi(\nabla\mathbf{v}) : (\nabla\nabla\psi) - \phi\mathbf{v} \cdot \nabla\omega\}, \quad (\text{B1})
 \end{aligned}$$

where we have introduced the following notation:

$$\overleftrightarrow{T} : \overleftrightarrow{U} \equiv T_{ij}U_{ij}. \quad (\text{B2})$$

As already mentioned in Sec. III C, we used a pseudospectral method to calculate Eq. (B1). In this method, the stream function ψ is expanded in Fourier series:

$$\psi = \sum_{\mathbf{k}} \hat{\psi}_{\mathbf{k}} e^{i\mathbf{k}\cdot\mathbf{r}}. \quad (\text{B3})$$

Substituting Eq. (B3) into Eq. (B1), we obtain

$$\begin{aligned}
 \frac{d\hat{\psi}_{\mathbf{k}}}{dt} = & -\frac{1}{k^2} \int_0^{2\pi} \\
 & \times \int_0^{2\pi} \frac{dx dy}{(2\pi)^2} (\text{r.h.s. of Eq. (B1)}) e^{-i\mathbf{k}\cdot\mathbf{r}}. \quad (\text{B4})
 \end{aligned}$$

APPENDIX C: NONSLIP LIMIT

To confirm that our model gives the nonslip boundary condition when $\xi \rightarrow \infty$, we performed simulations in G1 geometry with large values of ξ and typical values of other parameters. The result (the time evolution of $\langle v^{\text{tan}} \rangle$) is shown in Fig. 20. The amplitude of $\langle v^{\text{tan}} \rangle$ decreases as the drag coefficient ξ increases. For sufficiently large values of ξ/v_0 ($\gtrsim 1.0$), the slip velocity becomes almost zero, i.e., the boundary condition reduces to (almost) nonslip.

APPENDIX D: THRESHOLD VALUE OF λ_0 BELOW WHICH EDGE CURRENT OSCILLATION DOES NOT OCCUR

In Sec. IV C, we confirmed the absence of edge current oscillation when $\lambda_0 = 0$ and its presence when $\lambda_0 \geq 2.0$. Here, one question arises: Is there a finite threshold value of λ_0 , λ_0^{th} , below which the edge current oscillation does not occur?

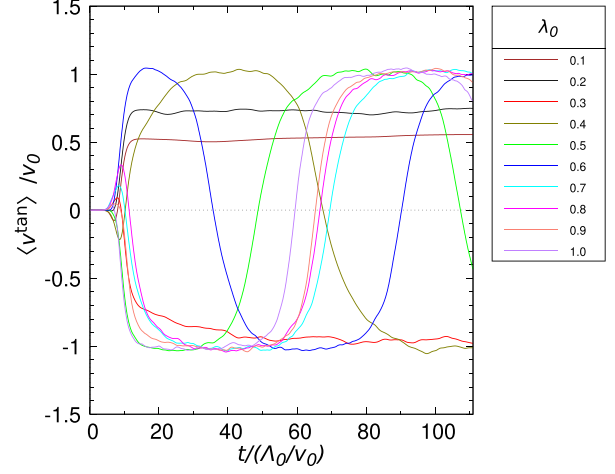


FIG. 21. Time evolution of $\langle v^{\text{tan}} \rangle$ for smaller values of λ_0 . Parameters other than those in Table I are as follows: $h/(\Lambda_0/v_0) = 0.000555$, $R/\Lambda_0 = 6.3$, and $\xi/v_0 = 2.8 \times 10^{-3}$.

Let us identify λ_0^{th} for a typical set of parameter values in this Appendix. To identify λ_0^{th} , we performed simulations in G1 geometry, varying the value of λ_0 from 0.1 to 1.9 at 0.1 intervals. The result (the time evolution of $\langle v^{\text{tan}} \rangle$) is shown in Fig. 21. Although we plot the results only for $0.1 \leq \lambda_0 \leq 1.0$ for clarity, we confirmed the oscillation for $1.1 \leq \lambda_0 \leq 1.9$. From Fig. 21, we can identify the threshold value as

$$0.3 < \lambda_0^{\text{th}} < 0.4. \quad (\text{D1})$$

APPENDIX E: THE BEHAVIOR IN A NARROW CHANNEL

In Refs. [32,33], active nematics are confined in G3 geometry. In these studies, when the distance between parallel walls is larger than the orientation correlation length, the particles near the edge align parallel with the wall while particles in the bulk have different directions. On the other hand, when the distance between walls is equal to or smaller than the orientation correlation length, the particles in the whole region have the direction parallel with the walls, which is called perfect order.

In our simulations, when the distance between the walls is large, the bulk region exhibits a turbulent behavior (see Figs. 13 and 14). This behavior is similar to the ones in Refs. [32,33]. When the distance between the walls is small, vortices line up at regular intervals ($\sim \Lambda_0$) in the y direction (see Figs. 22 and 23) and the perfect order observed in Refs. [32,33] does not emerge.

This difference can be explained as follows. In the simulations in Ref. [33], the emergence of perfect order is attributed to the nematic interaction between the constituent rodlike particles, which allows the orientational order near the walls to propagate into the channel center. On the other hand, in the TTSH simulation, the Swift-Hohenberg term that dictates the typical length scale of the spatial pattern destroys the uniform profile of \mathbf{v} , which results in the alternate distribution of clockwise and counter-clockwise vortices in the y direction. Thus, the difference in the behavior of order mentioned above is associated with the difference in how the order is generated.

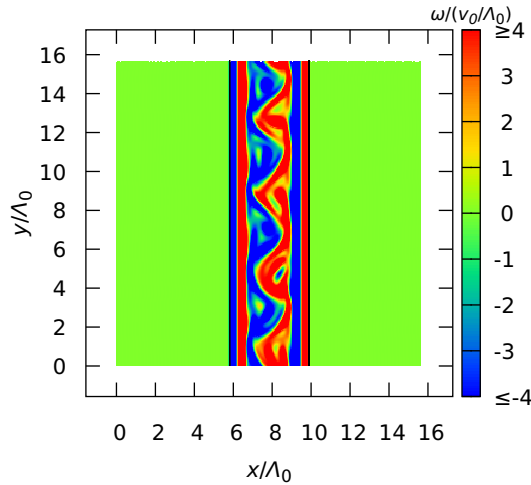


FIG. 22. A typical simulation snapshot of the vorticity field $\omega/(v_0/\Lambda_0) = (\nabla \times \mathbf{v})_z/(v_0/\Lambda_0)$ at the time $t/(\Lambda_0/v_0) = 274.6$ for G3 geometry. Parameters other than those in Table I are as follows: time increment $h/(\Lambda_0/v_0) = 0.000370$, $\lambda_0 = 4.0$, $R/\Lambda_0 = 1.6$, and $\xi/v_0 = 2.8 \times 10^{-2}$. Note that the spacing of two walls is $2R/\Lambda_0$. The black line indicates the outer edge of the smoothed boundary.

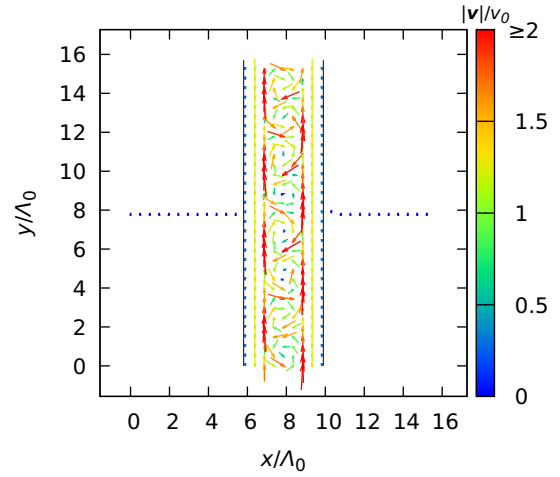


FIG. 23. A typical simulation snapshot of the velocity field \mathbf{v}/v_0 at the time $t/(\Lambda_0/v_0) = 274.6$ for G3 geometry. Parameters other than those in Table I are the same as in Fig. 22. The black line indicates the outer edge of the smoothed boundary. Velocity arrows are drawn at intervals of eight lattice points in each direction.

- [1] R. Alert, J. Casademunt, and J.-F. Joanny, Active turbulence, *Annu. Rev. Condens. Matter Phys.* **13**, 143 (2022).
- [2] A. Creppy, O. Praud, X. Druart, P. L. Kohnke, and F. Plouraboué, Turbulence of swarming sperm, *Phys. Rev. E* **92**, 032722 (2015).
- [3] D. Nishiguchi and M. Sano, Mesoscopic turbulence and local order in Janus particles self-propelling under an ac electric field, *Phys. Rev. E* **92**, 052309 (2015).
- [4] S.-Z. Lin, W.-Y. Zhang, D. Bi, B. Li, and X.-Q. Feng, Energetics of mesoscale cell turbulence in two-dimensional monolayers, *Commun. Phys.* **4**, 21 (2021).
- [5] P. Guillamat, J. Ignés-Mullol, and F. Sagués, Taming active turbulence with patterned soft interfaces, *Nat. Commun.* **8**, 564 (2017).
- [6] B. Martínez-Prat, R. Alert, F. Meng, J. Ignés-Mullol, J.-F. Joanny, J. Casademunt, R. Golestanian, and F. Sagués, Scaling regimes of active turbulence with external dissipation, *Phys. Rev. X* **11**, 031065 (2021).
- [7] H. H. Wensink, J. Dunkel, S. Heidenreich, K. Drescher, R. E. Goldstein, H. Löwen, and J. M. Yeomans, Meso-scale turbulence in living fluids, *Proc. Natl. Acad. Sci. USA* **109**, 14308 (2012).
- [8] J. Dunkel, S. Heidenreich, K. Drescher, H. H. Wensink, M. Bär, and R. E. Goldstein, Fluid dynamics of bacterial turbulence, *Phys. Rev. Lett.* **110**, 228102 (2013).
- [9] S. Heidenreich, J. Dunkel, S. H. L. Klapp, and M. Bär, Hydrodynamic length-scale selection in microswimmer suspensions, *Phys. Rev. E* **94**, 020601(R) (2016).
- [10] H. Reinken, S. H. L. Klapp, M. Bär, and S. Heidenreich, Derivation of a hydrodynamic theory for mesoscale dynamics in microswimmer suspensions, *Phys. Rev. E* **97**, 022613 (2018).
- [11] H. Wioland, F. G. Woodhouse, J. Dunkel, and R. E. Goldstein, Ferromagnetic and antiferromagnetic order in bacterial vortex lattices, *Nat. Phys.* **12**, 341 (2016).
- [12] K. Beppu, Z. Izri, J. Gohya, K. Eto, M. Ichikawa, and Y. T. Maeda, Geometry-driven collective ordering of bacterial vortices, *Soft Matter* **13**, 5038 (2017).
- [13] D. Nishiguchi, I. S. Aranson, A. Snezhko, and A. Sokolov, Engineering bacterial vortex lattice via direct laser lithography, *Nat. Commun.* **9**, 4486 (2018).
- [14] H. Reinken, D. Nishiguchi, S. Heidenreich, A. Sokolov, M. Bär, S. H. L. Klapp, and I. S. Aranson, Organizing bacterial vortex lattices by periodic obstacle arrays, *Commun. Phys.* **3**, 76 (2020).
- [15] H. Reinken, S. Heidenreich, M. Bär, and S. H. L. Klapp, Ising-like critical behavior of vortex lattices in an active fluid, *Phys. Rev. Lett.* **128**, 048004 (2022).
- [16] L. Puggioni, G. Boffetta, and S. Musacchio, Giant vortex dynamics in confined bacterial turbulence, *Phys. Rev. E* **106**, 055103 (2022).
- [17] L. Puggioni, G. Boffetta, and S. Musacchio, Flocking turbulence of microswimmers in confined domains, *Phys. Rev. E* **107**, 055107 (2023).
- [18] S. Shiratani, K. A. Takeuchi, and D. Nishiguchi, Route to turbulence via oscillatory states in polar active fluid under confinement, [arXiv:2304.03306](https://arxiv.org/abs/2304.03306).
- [19] K. Beppu, Z. Izri, T. Sato, Y. Yamanishi, Y. Sumino, and Y. T. Maeda, Edge current and pairing order transition in chiral bacterial vortices, *Proc. Natl. Acad. Sci. USA* **118**, e2107461118 (2021).
- [20] L. Yamauchi, T. Hayata, M. Uwamichi, T. Ozawa, and K. Kawaguchi, Chirality-driven edge flow and non-Hermitian topology in active nematic cells, [arXiv:2008.10852](https://arxiv.org/abs/2008.10852).

- [21] V. Yashunsky, D. J. G. Pearce, C. Blanch-Mercader, F. Ascione, P. Silberzan, and L. Giomi, Chiral edge current in nematic cell monolayers, *Phys. Rev. X* **12**, 041017 (2022).
- [22] B. C. van Zuiden, J. Paulose, W. T. M. Irvine, D. Bartolo, and V. Vitelli, Spatiotemporal order and emergent edge currents in active spinner materials, *Proc. Natl. Acad. Sci. USA* **113**, 12919 (2016).
- [23] V. Soni, E. S. Bililign, S. Magkiriadou, S. Sacanna, D. Bartolo, M. J. Shelley, and W. Irvine, The odd free surface flows of a colloidal chiral fluid, *Nat. Phys.* **15**, 1188 (2019).
- [24] H. Wioland, F. G. Woodhouse, J. Dunkel, J. O. Kessler, and R. E. Goldstein, Confinement stabilizes a bacterial suspension into a spiral vortex, *Phys. Rev. Lett.* **110**, 268102 (2013).
- [25] Y. Nakayama and R. Yamamoto, Simulation method to resolve hydrodynamic interactions in colloidal dispersions, *Phys. Rev. E* **71**, 036707 (2005).
- [26] M. Kanke and K. Sasaki, Equilibrium configuration in a nematic liquid crystal droplet with homeotropic anchoring of finite strength, *J. Phys. Soc. Jpn.* **82**, 094605 (2013).
- [27] J. Neustupa and P. Penel, The Navier-Stokes equation with slip boundary conditions (Mathematical Analysis in Fluid and Gas Dynamics), *RIMS Kôkyûroku* **1536**, 46 (2007), <http://hdl.handle.net/2433/59018>.
- [28] R. Ramaswamy and F. Jülicher, Activity induces traveling waves, vortices and spatiotemporal chaos in a model actomyosin layer, *Sci. Rep.* **6**, 1 (2016).
- [29] C. Canuto, M. Y. Hussaini, A. Quarteroni, and T. A. Zang, *Spectral Methods in Fluid Dynamics* (Springer, Berlin, Heidelberg, 1988).
- [30] See Supplemental Material at <http://link.aps.org/supplemental/10.1103/PhysRevE.109.054604> for the time evolution of the vorticity and velocity field. G1_vorticity.gif and G1_velocity.gif show the time evolution of the vorticity and velocity field, respectively, in G1 geometry. The same applies to G2 and G3 geometries. Parameters used for G1, G2, and G3 geometries are the same as in Figs. 1, 10, and 13, respectively.
- [31] J. Dunkel, S. Heidenreich, M. Bär, and R. E. Goldstein, Minimal continuum theories of structure formation in dense active fluids, *New J. Phys.* **15**, 045016 (2013).
- [32] G. Duclos, S. Garcia, H. G. Yevick, and P. Silberzan, Perfect nematic order in confined monolayers of spindle-shaped cells, *Soft Matter* **10**, 2346 (2014).
- [33] X. Li, R. Balagam, T.-F. He, P. P. Lee, O. A. Igoshin, and H. Levine, On the mechanism of long-range orientational order of fibroblasts, *Proc. Natl. Acad. Sci. USA* **114**, 8974 (2017).

Correction: The previously published Figures 8, 9, 16, 17, 18, and 19 contained incorrect labels on the vertical axes and have been replaced. Correspondingly, the value given for ω_c for G3 in the last paragraph of Sec. IV D has been fixed. A minor error in the seventh sentence of the penultimate paragraph of Sec. IV C has been rectified.